

## Hydrodynamic and Ballistic Transport over Large Length Scales in GaAs/AlGaAs

Adbhut Gupta<sup>1</sup>, J. J. Heremans<sup>1,\*</sup>, Gitansh Kataria<sup>2</sup>, Mani Chandra<sup>2,†</sup>, S. Fallahi<sup>3,4</sup>,  
G. C. Gardner<sup>4,5</sup> and M. J. Manfra<sup>3,4,5,6,7</sup>

<sup>1</sup>*Department of Physics, Virginia Tech, Blacksburg, Virginia 24061, USA*

<sup>2</sup>*Research Division, Quazar Technologies, Sarvapriya Vihar, New Delhi 110016, India*


<sup>3</sup>*Department of Physics and Astronomy, Purdue University, West Lafayette, Indiana 47907, USA*

<sup>4</sup>*Birck Nanotechnology Center, Purdue University, West Lafayette, Indiana 47907, USA*

<sup>5</sup>*Microsoft Quantum Purdue, Purdue University, West Lafayette, Indiana 47907, USA*

<sup>6</sup>*School of Electrical and Computer Engineering, Purdue University, West Lafayette, Indiana 47907, USA*

<sup>7</sup>*School of Materials Engineering, Purdue University, West Lafayette, Indiana 47907, USA*

 (Received 26 November 2019; revised 9 November 2020; accepted 21 January 2021; published 18 February 2021)

We study hydrodynamic and ballistic transport regimes through nonlocal resistance measurements and high-resolution kinetic simulations in a mesoscopic structure on a high-mobility two-dimensional electron system in a GaAs/AlGaAs heterostructure. We evince the existence of collective transport phenomena in both regimes and demonstrate that negative nonlocal resistances and current vortices are not exclusive to only the hydrodynamic regime. The combined experiments and simulations highlight the importance of device design, measurement schemes, and one-to-one modeling of experimental devices to demarcate various transport regimes.

DOI: [10.1103/PhysRevLett.126.076803](https://doi.org/10.1103/PhysRevLett.126.076803)

Electron transport in metals is often governed by momentum dissipation from electrons to the lattice, e.g., via impurity or phonon scattering. Such diffusive transport occurs when the momentum-relaxing (MR) electron mean-free path  $\ell_{\text{MR}}$  (obtained from electron mobility) is the shortest length scale in the system. However, in ultraclean two-dimensional electron systems (2DESs), a departure from diffusive transport occurs due to a long  $\ell_{\text{MR}}$ , giving rise to either ballistic or hydrodynamic transport [1]. In the ballistic regime, scattering mainly arises at the device boundaries, specularly or diffusively, and is delineated by the device scale  $W$  [2,3]. Yet inelastic electron-electron ( $e$ - $e$ ) interactions transfer momentum predominantly among the electrons instead of to the lattice, conserving momentum within the electron system. When such momentum-conserving (MC) scattering—characterized by MC scattering mean-free path  $\ell_{\text{MC}}$ —dominates, electrons can move collectively like a fluid and exhibit several effects associated with fluid dynamics [1,4–13]. The observation of this hydrodynamic regime in electronic systems has attracted significant interest [14–29].

The hydrodynamic regime shows a nonlocal current-voltage relation in devices, which can result in a negative nonlocal resistance ( $R_{\text{nl}}$ ) [6–10]. Such sign reversal has been exploited in recent experiments to detect the onset of the hydrodynamic regime [19–23]. However, the ballistic regime *also* shows a nonlocal current-voltage relation, and can likewise produce negative  $R_{\text{nl}}$  [10,11]. In fact, the ballistic regime also supports striking current vortices and collective motion of particles usually associated with fluid

depictions [30]. In this Letter, we reveal notable current vortices in both hydrodynamic and ballistic regimes, uniquely supported by evidence from elaborate measurements of  $R_{\text{nl}}$ . The presence of vortices in both hydrodynamic and ballistic regimes can be traced to electron momentum conservation in both regimes [10,30].

We present strides in experimental device design, measurement schemes, and concomitant results, as well as in one-to-one modeling of the experimental device, pivotal in demarcating the transport regimes. We demonstrate measurements of  $R_{\text{nl}}$  in a large-scale ( $\sim 30 \times 24 \mu\text{m}$ ) ultraclean ( $\ell_{\text{MR}} \simeq 65 \mu\text{m}$  at 4.2 K) device, which by its scale offers exceptional sensitivity to MC scattering and hosts 10 point contacts (PCs) to probe voltages at various distances  $\Delta x$  between the current injection point and voltage probes [Figs. 1(a) and 1(b)]. The measurements at various  $\Delta x$  are critical to check against the predictions of ballistic or hydrodynamic models. The exceptionally long  $\ell_{\text{MR}}$ , due to optimized GaAs/AlGaAs MBE growth, favors the appearance of nondiffusive transport regimes. We interpret the experimental results using realistic high-resolution simulations of quasiparticle transport at the kinetic level, involving the actual experimental geometry in the precise contact configuration and taking into account both MR and MC scattering. The simulations with  $\ell_{\text{MR}}$  and  $\ell_{\text{MC}}$  as inputs determine that the device transitions from a predominantly ballistic regime at  $T = 4.2$  K to a hydrodynamic regime at  $T \approx 12$ – $19$  K [Fig. 1(c)].

Mesoscopic geometries were patterned on a GaAs/AlGaAs heterostructure containing a 2DES with

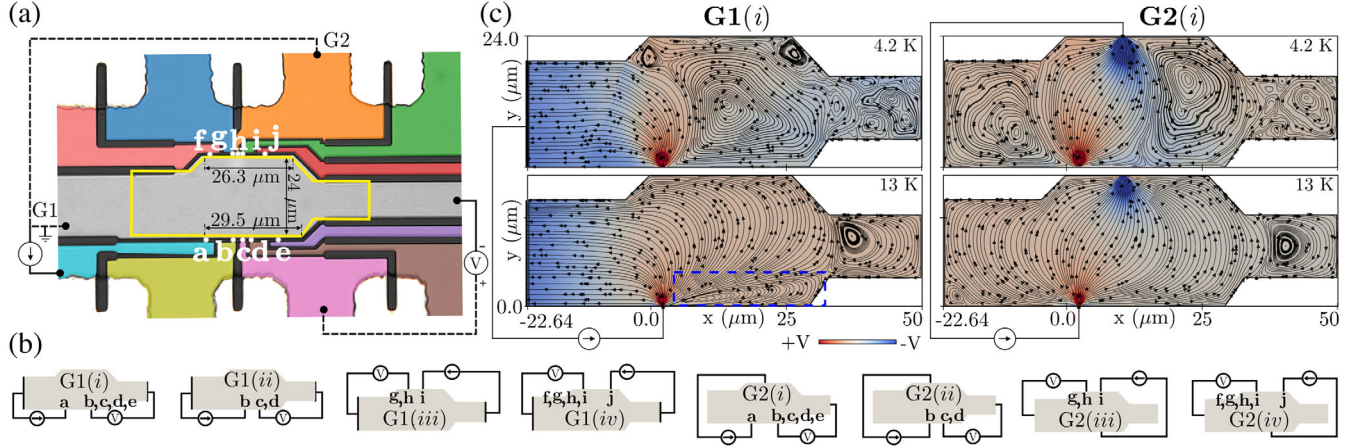


FIG. 1. (a) Optical micrograph of the geometry showing dimensions, PCs  $a$ – $j$  (indicated by white dots, with paths to PCs in distinct colors), the computational domain (yellow outline), and current and voltage PCs, for example, measurements in the G1( $i$ ) and G2( $i$ ) configurations. Unused PCs are left floating. (b) Schematics of subconfigurations G1( $i$ – $iv$ ) and G2( $i$ – $iv$ ) depending on current injection PC and voltage measurement PC. (c) Simulated current streamline and voltage contour plots for G1( $i$ ) and G2( $i$ ) at  $T = 4.2$  and 13 K. The streamline and source arrows depict the direction of conventional current.

mobility  $\mu$  exceeding  $670 \text{ m}^2/(\text{V s})$  at 4.2 K. The areal electron density is  $n_S \approx 3.4 \times 10^{15} \text{ m}^{-2}$ , corresponding to a Fermi energy  $E_F \approx 11.2 \text{ meV}$  and  $\ell_{\text{MR}} = 64.5 \text{ }\mu\text{m}$  at 4.2 K (Supplemental Material Sec. 1 [31]). To measure  $R_{\text{nl}}$ , we fabricated an in-line mesoscopic geometry [Fig. 1(a)] containing 10 PCs ( $a$ – $j$ ) located in barriers, which are on both sides of a multiterminal Hall mesa, with sides separated by  $W \approx 24 \text{ }\mu\text{m}$ . Each PC can act as either a current injector  $\alpha$  (injecting electrons) or a voltage detector  $\beta$  (detecting a nonlocal voltage). A measurement is defined by a pair consisting of an injector PC  $\alpha$  and a detector PC  $\beta$  in the same barrier, and we label the center-to-center separation between PCs in such pair as  $L_{\alpha\beta}$ , where  $L_{\alpha\beta}$  ranges from 1.3 to  $20.5 \text{ }\mu\text{m}$ . Calling  $V_{\text{nl}}$  the nonlocal voltage measured at  $\beta$  vs a faraway counterprobe if current  $I$  is injected at  $\alpha$  and drained at another faraway counterprobe [Fig. 1(a)], the four-probe nonlocal resistance is expressed as  $R_{\text{nl}} = V_{\text{nl}}/I$  and  $R_{\text{nl}}$  takes the sign of  $V_{\text{nl}}$ . Measurements were performed in the linear response regime, i.e., for small excitation energies (such that the system is everywhere close to equilibrium, with electrons close to  $E_F$ ) over  $4.2 \leq T \leq 40 \text{ K}$ , using low-frequency ( $\sim 44 \text{ Hz}$ ) ac lock-in techniques without dc offsets. We use  $I \sim 200 \text{ nA}$ , which is large enough for formation of vortices (Supplemental Material Sec. 4 [31]), yet small enough to avoid electron heating. The conducting PC width  $w \approx 0.6 \text{ }\mu\text{m}$  and the Fermi wavelength  $\lambda_F = 43 \text{ nm}$  show that  $w/(\lambda_F/2) \approx 28$  spin-degenerate transverse modes contribute to transport, yielding a PC resistance  $\approx (h/2e^2)/28 = 461 \text{ }\Omega$  (Supplemental Material Sec. 1 [31]). The large number of modes implies that PCs are very much open and act as classical PCs. The barriers and boundaries were defined using wet etching, which results in predominantly specular boundary scattering [37,38].

We exploit the flexibility provided by the geometry, allowing testing of different configurations for current injector and drain, and for many  $\Delta x$ , in the *same* device. We use two current configurations: G1 where, after injection at  $\alpha$ ,  $I$  is drained at the side of the device, and G2 where  $I$  is drained at a PC at the opposite side of the device [Figs. 1(a) and 1(b)]. The sensitivity to MC scattering turns out much higher in G1 (vicinity geometry [20]) than in G2 (Supplemental Material Sec. 7 [31]).

Transport in the device is modeled via the Boltzmann equation [10,31]

$$\frac{1}{v_F} \frac{\partial f}{\partial t} + \left( \frac{\mathbf{p}}{mv_F} \right) \cdot \frac{\partial f}{\partial \mathbf{x}} = -\frac{f - f_0^{\text{MR}}}{\ell_{\text{MR}}} - \frac{f - f_0^{\text{MC}}}{\ell_{\text{MC}}}, \quad (1)$$

where  $f(\mathbf{x}, \mathbf{p}, t)$  is the electron distribution in the spatial coordinates  $\mathbf{x} \equiv (x, y)$ , momentum coordinates  $\mathbf{p} \equiv (p_x, p_y)$ , and time  $t$ . While long-range electric fields are not explicitly present in Eq. (1), they are included at linear order as the gradient of the electrochemical potential [10]. The left side (with  $v_F$  as the Fermi velocity and  $m$  as the effective mass) describes free advection, and the right side describes thermalization due to MR and MC scattering in a relaxation time approximation [39] with  $f_0^{\text{MR}}$  and  $f_0^{\text{MC}}$  as the local stationary and drifting Fermi-Dirac distributions (details of the model can be found in [10] and in the Supplemental Material Sec. 2 [31]). The model inputs are  $\ell_{\text{MC}}$  (a free parameter) and  $\ell_{\text{MR}}$  (fixed by  $\mu$ ). We consider dynamics at the Fermi surface without thermal smearing so that  $\mathbf{p} = mv_F \hat{p}$  and solve for transport in the zero-frequency limit ( $\partial/\partial t \rightarrow 0$ );  $v_F$  then factors out, leaving the circular Fermi contour as the only relevant detail. We solve Eq. (1) in the precise experimental geometry using BOLT [40], a high-resolution solver for kinetic

theories. The overall prefactor of the numerical solutions is set by calibrating against the measurements in G1(ii) [Fig. 1(b)] for each  $T$  (Supplemental Material Sec. 3 [31]).

The experimental  $R_{nl}$  vs  $T$  for G1 and G2 are depicted in Figs. 2(a) and 2(b), respectively, for the specific  $L_{\alpha\beta}$  used in measurements [Fig. 1(a) exemplifies  $L_{ac}$ ]. Two inferences appear: the negative  $R_{nl}$  attest to a departure from diffusive transport, and a striking contrast exists in  $T$  dependences between G1 and G2. For G1,  $R_{nl}$  shows a nonmonotonic dependence on  $T$ , initially decreasing as  $T$  increases, crossing over to negative values in a particular range of  $T$  for given  $L_{\alpha\beta}$ , then increasing to positive values. For G2,  $R_{nl}$  increases from negative values at low  $T$  to positive values at higher  $T$ . The difference in  $T$  dependence between G1 and G2 indicates that the current injector-drain configuration significantly affects transport. Figure 2(a) can be directly compared with similar results in graphene [20,22] and other GaAs/AlGaAs experiments [19]. Figures 2(c) and 2(d) depict  $R_{nl}$  vs  $\Delta x$  parametrized in

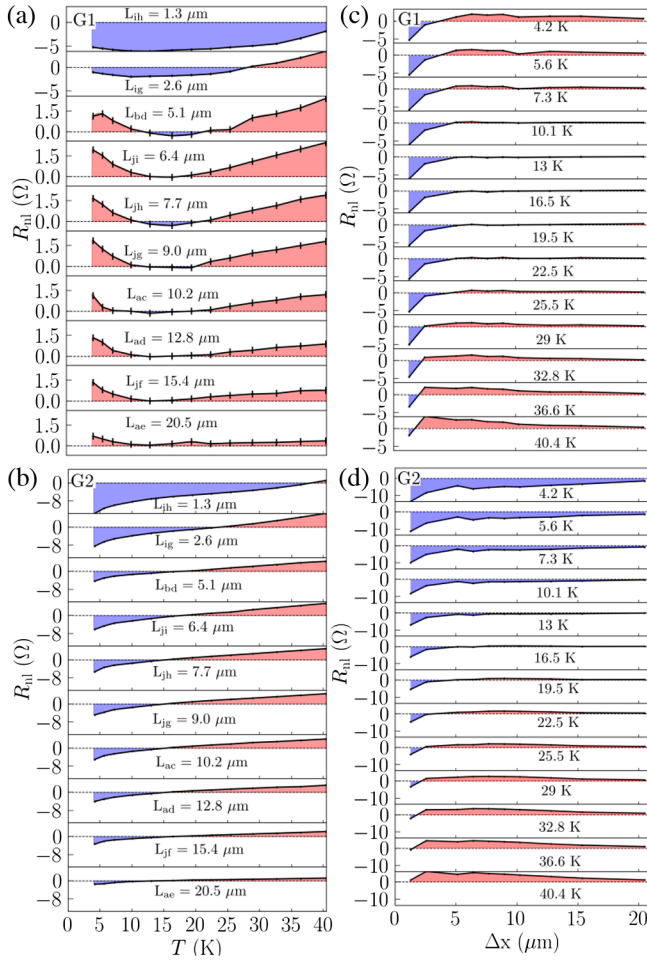


FIG. 2. (a),(b) Experimental nonlocal resistance  $R_{nl}$  vs  $T$  for each  $L_{\alpha\beta}$  for (a) G1 and (b) G2. (c),(d)  $R_{nl}$  vs  $\Delta x$  for each  $T$  for (c) G1 and (d) G2. The dotted lines indicate  $R_{nl} = 0$ , with negative (positive) regions of  $R_{nl}$  shaded in blue (red).

$T$  for G1 and G2, respectively, tracing a crossover from negative to positive values vs  $\Delta x$ .

In Fig. 2(a) for  $T \lesssim 10$  K, G1 shows negative  $R_{nl}$  for small  $\Delta x \lesssim 2.6 \mu\text{m}$  ( $L_{ih}, L_{ig}$ ), crossing over to positive  $R_{nl}$  for  $\Delta x \gtrsim 5.1 \mu\text{m}$  ( $L_{bd}, L_{ji}, \dots$ ). As  $T$  is increased,  $R_{nl}$  vs  $T$  develops a minimum for all  $\Delta x$ , and the  $R_{nl}$  at this minimum crosses over to negative values for  $\Delta x \lesssim 12.8 \mu\text{m}$ . These observations [confirmed in Fig. 2(c)] are a consequence of the interplay between  $\ell_{MC}(T)$ ,  $\ell_{MR}(T)$ , and geometry. Considering only  $\ell_{MR}(T)$ , with  $\ell_{MR}(4.2\text{K}) = 64.5 \mu\text{m} \gg W = 24 \mu\text{m}$  at  $T = 4.2$  K, the system is predominantly ballistic. By finding the values of  $\ell_{MC}$  (used as a model input parameter, given  $\ell_{MR}$ ) for which the experimental and modeled  $R_{nl}$  match, we have a means of bracketing values for  $\ell_{MC}(T)$ . The procedure is illustrated in Fig. 3. In Fig. 3(a) we focus on  $T = 4.2$  K, lying in the region  $T \lesssim 10$  K showing a crossover vs  $\Delta x$  from negative  $R_{nl}$  at small  $\Delta x$  (1.3 and 2.6  $\mu\text{m}$ ) to positive further away [see Figs. 2(a) and 2(c)]. The inset in Fig. 3(a) (panel 3) shows that the limiting billiard model, common in ballistic transport and using ( $\ell_{MC} \rightarrow \infty, \ell_{MR} \rightarrow \infty$ ), does not capture the crossover vs  $\Delta x$  because it results in  $R_{nl} > 0$  for all  $\Delta x$  (inset, black trace); yet positive  $R_{nl}$  is not universal in the billiard model and can be heavily influenced by geometry (Supplemental Material Sec. 6 [31]). Introducing finite MR scattering via the experimental  $\ell_{MR} = 64.5 \mu\text{m}$  ( $T = 4.2$  K) and zero MC scattering with  $\ell_{MC} \rightarrow \infty$ , the modeled  $R_{nl}$  are lower compared to the billiard model but *still* do not reach  $R_{nl} < 0$  at small  $\Delta x$  (inset, blue trace). As shown in Fig. 3(a), only with finite MC scattering using a range  $\ell_{MC} \approx 60\text{--}300 \mu\text{m}$  ( $\gg W = 24 \mu\text{m}$ ), does the model yield a crossover from negative to positive  $R_{nl}$  with increasing  $\Delta x$ . The inset in Fig. 3(b) (panel 2) plots this range at 4.2 K as compatible with data and model.

A theoretical prediction for  $\ell_{MC}$  is found in a commonly used theoretical expression for quantum lifetime by Giuliani and Quinn (GQ) [36] [Eq. (S1) in Supplemental Material Sec. 5 [31]], also plotted in the inset. The inset demonstrates that  $\ell_{MC} \approx 60\text{--}300 \mu\text{m}$  exceeds values from GQ which at 4.2 K yields  $\ell_{MC} \approx 15 \mu\text{m}$ . In fact, using  $\ell_{MC} = 15 \mu\text{m}$  in the model yields  $R_{nl} < 0$  throughout the device [Fig. 3(a), green curve], contrary to experimental observations. Recent results, in fact, suggest that longer  $\ell_{MC}$  can result from dielectric screening [27]. In short, considering  $\ell_{MC}$ , for  $T \lesssim 10$  K neither the billiard model ( $\ell_{MC} \rightarrow \infty$ ) nor GQ (too short  $\ell_{MC}$ ) reproduce the experiments, and intermediate  $\ell_{MC}$  is required. Further, the presence of numerous current vortices of various sizes in the predominantly ballistic regime [Fig. 1(c) at 4.2 K] reveals that dominance of MC scattering is not obligatory for the formation of vortices.

For  $10 \lesssim T \lesssim 22.5$  K in G1,  $R_{nl}$  vs  $T$  develops a minimum, which becomes shallower with increasing  $\Delta x$ , and  $R_{nl}$  crosses over to negative values for  $\Delta x \lesssim 12.8 \mu\text{m}$

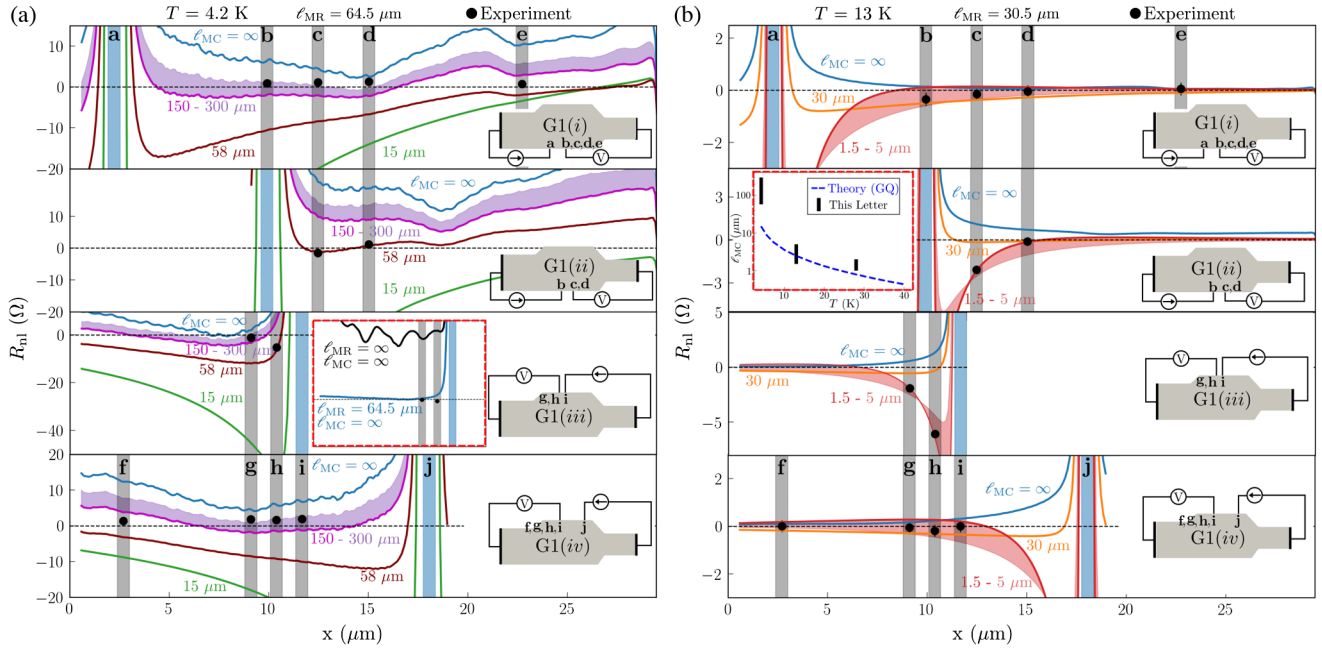


FIG. 3. Experimental  $R_{nl}$  (black dots) and modeled  $R_{nl}$  (lines) for G1(*i-iv*), plotted vs location  $x$  along the barrier into which the injection PC (blue vertical bars) is placed, at (a)  $T = 4.2$  K where  $\ell_{MR} = 64.5 \mu\text{m}$  and (b)  $T = 13$  K where  $\ell_{MR} = 30.5 \mu\text{m}$ . The modeled  $R_{nl}$  (lines) is shown parametrized in  $\ell_{MC}$ . Schematics of subconfigurations are also depicted. The gray vertical bars represent locations of detector PCs. Experimental  $R_{nl}$  (black dots) for G1(*ii*) are chosen for reference calibration (Supplemental Material Sec. 3 [31]) given the clear crossover in  $R_{nl}$  in G1(*ii*). Inset in (a) (panel 3) shows  $R_{nl}$  for G1(*iii*) for ( $\ell_{MC} \rightarrow \infty, \ell_{MR} \rightarrow \infty$ ) and for ( $\ell_{MC} \rightarrow \infty, \ell_{MR} = 64.5 \mu\text{m}$ ). Inset in (b) (panel 2) shows the extracted  $\ell_{MC}$  vs  $T$  (black bars), along with theoretical estimates (blue dotted line) from GQ [36] [Eq. (S1) in Supplemental Material Sec. 5 [31]].

[Fig. 2(a)]. Modeling using  $\ell_{MC} \simeq 1.5\text{--}5 \mu\text{m}$  accommodates all the experimental data at  $T = 13$  K [Fig. 3(b)]. Since  $\ell_{MC} \ll W$  and  $\ell_{MC} \ll \ell_{MR}$  while  $\ell_{MR} = 30.5 \mu\text{m} \gtrsim W$  is sufficiently long, the system is in the hydrodynamic regime. At  $T = 13$  K, GQ yields  $\ell_{MC} \simeq 2.5 \mu\text{m}$  [36], lying in the model's range of  $\ell_{MC} \simeq 1.5\text{--}5 \mu\text{m}$ . This suggests that using conditions where  $\ell_{MC} \gtrsim W$  (as at 4.2 K) leads to a more discriminating test of microscopic theories of  $\ell_{MC}$ . As expected in the hydrodynamic regime, Fig. 1(c) (13 K) exhibits current vortices.

Yet the current vortices in the hydrodynamic regime in Fig. 1(c) (13 K) exhibit a distinct pattern compared to the ballistic vortices at 4.2 K. In the hydrodynamic regime only a single vortex [dashed box in Fig. 1(c)] inhabits the main chamber, and this result is obtainable from just the Navier-Stokes fluid equations. In contrast, the ballistic profile [top panels in Fig. 1(c)] shows multiple vortices, which cannot be accessed from fluid equations and require solving a Boltzmann kinetic equation. Notably, while the fluid equations cannot access the ballistic limit, the Boltzmann equation can access the fluid solutions in the limit  $\ell_{MC} \ll W$ .

As  $T$  is increased further in G1 to  $T \gtrsim 19$  K, Fig. 2(a) shows an upward trend in  $R_{nl}$  vs  $T$  toward  $R_{nl} > 0$  for all  $\Delta x$ . The crossover to  $R_{nl} > 0$  occurs at higher  $T$  for smaller  $\Delta x$  ( $R_{nl}$  at  $\Delta x = 1.3 \mu\text{m}$  is still negative at 40 K but is estimated to go positive around 45 K). This is corroborated

by Fig. 2(c) where the region of  $R_{nl} < 0$  diminishes to smaller  $\Delta x$  with increasing  $T$ . This behavior heralds a breakdown of hydrodynamic transport and a transition from hydrodynamic to diffusive dynamics as MR scattering increasingly affects transport. In G1 the hydrodynamic regime exists at intermediate  $T \approx 12\text{--}19$  K, estimated from Fig. 2(c) by tracing the crossover from negative to positive  $R_{nl}$  vs  $\Delta x$ . Supplemental Material Sec. 8 [31] shows the experimental and modeled  $R_{nl}$  at 28 K and the change in vortex pattern with changing  $\ell_{MC}$ .

Figures 2(b) and 2(d) reveal that in the G2 configuration  $R_{nl} < 0$  occurs over a wide range of  $T$ , rendering it inefficient in differentiating between ballistic and hydrodynamic regimes. The simulations also show that G2 is *insensitive* to MC scattering (Supplemental Material Sec. 7 [31]). Both properties disallow using G2 to determine  $\ell_{MC}$ , highlighting the importance of choosing appropriate contact configurations for discriminating transport regimes.

In conclusion, nondiffusive transport, either predominantly ballistic or hydrodynamic, is realized over a wide temperature range in a large-scale GaAs/AlGaAs geometry. The appearance of both predominantly ballistic or hydrodynamic regimes at such a large scale, despite opposite required limits of the strength of MC scattering, is striking. Equally remarkable are their shared characteristics of negative nonlocal resistances and current vortices. The nonlocal resistance in both regimes can be tuned by

device and contact geometry, used here to disentangle the regimes and to obtain a measure of the MC scattering length. While the importance of geometry in the ballistic regime is well known, we additionally find that the ballistic regime can also exhibit collective effects, such as current vortices, even in the absence of dominant electron-electron interactions in a large-scale ultraclean device.

The authors acknowledge support by the U.S. Department of Energy, Office of Basic Energy Sciences, Division of Materials Sciences and Engineering under Awards No. DE-FG02-08ER46532 (J.J.H.) and No. DE-SC0020138 (M.J.M.). The authors acknowledge computational resources (GPU clusters Cascades and NewRiver) and technical support provided by Advanced Research Computing at Virginia Tech. We thank Ravishankar Sundararaman for helpful discussions. M. C. thanks Sujit Kumar for hospitality during the course of this work.

\*heremans@vt.edu

†manic@illinois.edu

- [1] M. J. M. de Jong and L. W. Molenkamp, *Phys. Rev. B* **51**, 13389 (1995).
- [2] J. J. Heremans, M. B. Santos, and M. Shayegan, *Appl. Phys. Lett.* **61**, 1652 (1992).
- [3] J. J. Heremans, M. B. Santos, K. Hirakawa, and M. Shayegan, *J. Appl. Phys.* **76**, 1980 (1994).
- [4] R. N. Gurzhi, *Sov. Phys. Usp.* **11**, 255 (1968).
- [5] A. O. Govorov and J. J. Heremans, *Phys. Rev. Lett.* **92**, 026803 (2004).
- [6] I. Torre, A. Tomadin, A. K. Geim, and M. Polini, *Phys. Rev. B* **92**, 165433 (2015).
- [7] F. M. D. Pellegrino, I. Torre, A. K. Geim, and M. Polini, *Phys. Rev. B* **94**, 155414 (2016).
- [8] L. Levitov and G. Falkovich, *Nat. Phys.* **12**, 672 (2016).
- [9] H. Guo, E. Ilseven, G. Falkovich and, and L. Levitov, *Proc. Natl. Acad. Sci. U.S.A.* **114**, 3068 (2017).
- [10] M. Chandra, G. Kataria, D. Sahdev, and R. Sundararaman, *Phys. Rev. B* **99**, 165409 (2019).
- [11] A. Shytov, J. F. Kong, G. Falkovich, and L. Levitov, *Phys. Rev. Lett.* **121**, 176805 (2018).
- [12] K. E. Nagaev, *Phys. Rev. B* **102**, 045426 (2020).
- [13] P. Ledwith, H. Guo, A. Shytov, and L. Levitov, *Phys. Rev. Lett.* **123**, 116601 (2019).
- [14] D. Taubert, G. J. Schinner, H. P. Tranitz, W. Wegscheider, C. Tomaras, S. Kehrein, and S. Ludwig, *Phys. Rev. B* **82**, 161416(R) (2010).
- [15] D. Taubert, G. J. Schinner, C. Tomaras, H. P. Tranitz, W. Wegscheider, and S. Ludwig, *J. Appl. Phys.* **109**, 102412 (2011).
- [16] P. J. W. Moll, P. Kushwaha, N. Nandi, B. Schmidt, and A. P. Mackenzie, *Science* **351**, 1061 (2016).
- [17] G. M. Gusev, A. D. Levin, E. V. Levinson, and A. K. Bakarov, *AIP Adv.* **8**, 025318 (2018).
- [18] B. A. Braem, F. M. D. Pellegrino, A. Principi, M. Rösli, C. Gold, S. Hannel, J. V. Koski, M. Berl, W. Dietsche, W. Wegscheider *et al.*, *Phys. Rev. B* **98**, 241304(R) (2018).
- [19] A. D. Levin, G. M. Gusev, E. V. Levinson, Z. D. Kvon, and A. K. Bakarov, *Phys. Rev. B* **97**, 245308 (2018).
- [20] D. A. Bandurin, I. Torre, R. K. Kumar, M. B. Shalom, A. Tomadin, A. Principi, G. H. Auton, E. Khestanova, K. S. Novoselov, I. V. Grigorieva *et al.*, *Science* **351**, 1055 (2016).
- [21] R. K. Kumar, D. A. Bandurin, F. M. D. Pellegrino, Y. Cao, A. Principi, H. Guo, G. H. Auton, M. B. Shalom, L. A. Ponomarenko, G. Falkovich *et al.*, *Nat. Phys.* **13**, 1182 (2017).
- [22] D. A. Bandurin, A. V. Shytov, L. S. Levitov, R. K. Kumar, A. I. Berdyugin, M. B. Shalom, I. V. Grigorieva, A. K. Geim, and G. Falkovich, *Nat. Commun.* **9**, 4533 (2018).
- [23] A. I. Berdyugin, S. G. Xu, F. M. D. Pellegrino, R. K. Kumar, A. Principi, I. Torre, M. B. Shalom, T. Taniguchi, K. Watanabe, I. V. Grigorieva *et al.*, *Science* **364**, 162 (2019).
- [24] V. Galitski, M. Kargarian, and S. Syzranov, *Phys. Rev. Lett.* **121**, 176603 (2018).
- [25] D. Svintsov, *Phys. Rev. B* **97**, 121405(R) (2018).
- [26] J. Gooth, F. Menges, N. Kumar, V. Süß, C. Shekhar, Y. Sun, U. Drechsler, R. Zierold, C. Felser, and B. Gotsmann, *Nat. Commun.* **9**, 4093 (2018).
- [27] M. Kim, S. G. Xu, A. I. Berdyugin, A. Principi, S. Slizovskiy, N. Xin, P. Kumaravadivel, W. Kuang, M. Hamer, R. K. Kumar *et al.*, *Nat. Commun.* **11**, 2339 (2020).
- [28] M. J. H. Ku, T. X. Zhou, Q. Li, Y. J. Shin, J. K. Shi, C. Burch, L. E. Anderson, A. T. Pierce, Y. Xie, A. Hamo *et al.*, *Nature (London)* **583**, 537 (2020).
- [29] O. E. Raichev, G. M. Gusev, A. D. Levin, and A. K. Bakarov, *Phys. Rev. B* **101**, 235314 (2020).
- [30] M. Chandra, G. Kataria, and D. Sahdev, [arXiv:1910.13737](https://arxiv.org/abs/1910.13737).
- [31] See Supplemental Material at <http://link.aps.org/supplemental/10.1103/PhysRevLett.126.076803> for 2DES properties, modeling calibration, conditions for vortices, effects of geometry and contact configuration, and effect of MR scattering at higher temperatures, which includes Refs. [7,10,32–36].
- [32] G. C. Gardner, S. Fallahi, J. D. Watson, and M. J. Manfra, *J. Cryst. Growth* **441**, 71 (2016).
- [33] W. Zawadzki and W. Szymańska, *Phys. Status Solidi B* **45**, 415 (1971).
- [34] W. Zawadzki, *J. Phys. Condens. Matter* **29**, 373004 (2017).
- [35] J. J. Harris, C. T. Foxon, D. Hilton, J. Hewett, C. Roberts, and S. Auzoux, *Surf. Sci.* **229**, 113 (1990).
- [36] G. F. Giuliani and J. J. Quinn, *Phys. Rev. B* **26**, 4421 (1982).
- [37] J. J. Heremans, S. von Molnár, D. D. Awschalom, and A. C. Gossard, *Appl. Phys. Lett.* **74**, 1281 (1999).
- [38] H. Chen, J. J. Heremans, J. A. Peters, A. O. Govorov, N. Goel, S. J. Chung, and M. B. Santos, *Appl. Phys. Lett.* **86**, 032113 (2005).
- [39] We restrict ourselves to solutions of the Boltzmann equation in which MC scattering is parametrized with a single relaxation timescale. References [12,13] report on transport phenomena that can result from a more sophisticated collision integral.
- [40] M. Chandra, S. Sankaran, and P. Yalamanchili, <https://www.github.com/mchandra/bolt>.